Published in final edited form as:
Science. 2008 August 29; 321(5893): 1210–1214. doi:10.1126/science.1159674.

A Structural Mechanism for MscS Gating in Lipid Bilayers

Valeria Vásquez[1,2], **Marcos Sotomayor**[3], **Julio Cordero-Morales**[1,2], **Klaus Schulten**[4], and **Eduardo Perozo**[2]

[1]Department of Molecular Physiology and Biological Physics. University of Virginia. Charlottesville, VA 22908

[2]Department of Biochemistry and Molecular Biology. Institute for Biophysical Dynamics. University of Chicago, IL 60637

[3]Howard Hughes Medical Institute and Department of Neurobiology, Harvard Medical School. Boston, MA 02115

[4]Department of Physics, University of Illinois at Urbana-Champaign, and Beckman Institute for Advanced Science and Technology. Urbana, IL 61801

Abstract

The mechanosensitive channel of small conductance (MscS) is a key determinant in the prokaryotic response to osmotic challenges. Here, we have determined the structural rearrangements associated with MscS activation in membranes using patch-clamp, EPR spectroscopy, and computational analyses. MscS was trapped in its open conformation after modifying the transbilayer pressure profile through the asymmetric incorporation of lysophospholipids. The transition from the closed to the open state is accompanied by the downward tilting of the TM1–TM2 hairpin, and by the expansion, tilt, and rotation of the TM3 helices. These movements expand the permeation pathway, leading to an increase in water accessibility around TM3. Our open MscS model is compatible with single channel conductance measurements and supports the notion that helix tilting is associated with efficient pore widening in mechanosensitive channels.

Mechanosensation is involved in many physiological roles, including osmotic balance, touch, and hearing (1,2). At the molecular level, mechanosensitivity relies on the activity of ion channels that transduce a variety of mechanical stimuli to open a conductive pore. Mechanosensitive (MS) channels are grouped by function rather than sequence similarity (3,4). In prokaryotic systems, MS channels respond directly to bilayer deformations, with a transduction mechanism defined at the protein-lipid interface (5,6). Although this is also true for some eukaryotic MS channels (7), many also respond to mechanical deformations through their association with the cytoskeletal network (8).

While the molecular identification of eukaryotic MS channels remains challenging (2,9,10), the biophysical and structural properties of prokaryotic MS channels have proved far more tractable at the molecular level. The crystal structures for the MS channels of large (MscL) and small (MscS) conductance (11–13), have provided a molecular framework to interpret functional and biophysical data and have helped establish the basic mechanistic principles by which these two distinct channels sense the physical state of the bilayer (14–17). Nevertheless, given the critical role that lipid-protein interactions play in prokaryotic

Correspondence should be addressed to E.P at eperozo@uchicago.edu.

Supporting Online Material Material and Methods Fig. S1 to S6

function (15), two questions arise: First, what is the correspondence between these crystal structures and mechanistically-defined functional states? Second, what are the conformational rearrangements underlying the transitions along the gating pathway?

Functional, spectroscopic, and computational studies have shown that in the pentameric MscL activation gating proceeds as a result of a large tilt of both transmembrane (TM) segments (14,17,18). Concerted helical rotation and tilting generates a large aqueous pore, much as in the iris of a camera lens. However, an equivalent gating mechanism is not as obvious in the case of MscS. With three TM segments arranged as a homoheptamer (12), the structural design of MscS is very different to that of MscL. Furthermore, while the MscL crystal structure appears to be a good representation of the closed conformation in its native environment (19,20), the functional state represented by the MscS crystal structure (12,13) has yet to be determined (21–26). Finally, in the presence of a sustained mechanical stimulus, MscS undergoes a desensitization/inactivation transition (22,27,28) that is not fully understood at the molecular level. Thus, while MscL and MscS respond to similar bilayer perturbations, the mechanism of transducing these forces might be different.

Electron paramagnetic resonance (EPR) measurements on a lipid-reconstituted closed state of MscS has provided direct evidence for a more compact TM domain arrangement than that seen in the crystal structure (21). In the closed conformation, the TM1 and TM2 segments realign 9° towards the normal of the membrane, allowing TM3 to further narrow the permeation path. Here, we have investigated how bilayer deformations trigger MscS opening. To this end, we have used site-directed spin-labeling and EPR spectroscopy to monitor the structural rearrangements in all three MscS TM segments, relative to the MscS crystal structure (12,13) and in comparison with our spectroscopic data in the closed state.

We used cone-shaped amphiphiles that modify the bilayer tension profile (7,15,29) to stabilize the open conformation of MscS (Fig. 1). As expected (22,28,30), application of a sustained negative pressure elicits the activation and subsequent inactivation of MscS (Fig. 1A). Even in the absence of an applied external pressure, perfusion with LPC micelles elicited spontaneous MscS openings (Fig. 1B) that displayed identical single channel properties as those activated by transbilayer pressure differences. Under these conditions, MscS channels can be continuously recruited by sequential incorporation of LPC, until the membrane seal breaks. Remarkably, we found no evidence of an LPC-induced desensitization/inactivation. This fortuitous observation makes LPC a very useful tool for the investigation of MscS in its open conformation by spectroscopic approaches. At the same time, this suggests that LPC incorporation might be exerting different bilayer perturbation forces to those of the better-characterized transbilayer pressure difference (31,32).

127 cysteine mutants (Fig. 2A), covering the N-terminal region and all TM segments (residues 2–128), were expressed, spin-labeled, and reconstituted into liposomes (21,33). Each labeled mutant was activated by incorporation of LPC (25 mol %) and EPR spectroscopic measurements were carried out on both the closed (21), and LPC-open conformations. Changes in probe mobility were evaluated from line-shape differences (ΔH_0^{-1}) and the accessibility to either the membrane lipid (ΠO_2) or the aqueous environment (ΠNiEdda) from power saturation experiments (34). Figure 2B shows spectra from residues lining the permeation pathway (L105C-SL to G113C-SL). The complete EPR environmental data set for the TM domain (Fig. 2C) shows that the transition to the open state in MscS is accompanied by smaller structural changes than those seen in the pentameric MscL (14). This is not unexpected, given the smaller single channel conductance of MscS (in respect to MscL) and the fact that small inter-subunit movements in the homoheptamer could generate the radial pore changes needed to support ion conduction.

Upon opening, both the N-terminus and the TM1–TM2 loop reduce their accessibility to the polar agent NiEdda. Given that the overall α-periodicity of the TM1 and TM2 is preserved (data not shown) the most parsimonious explanation for this change in accessibility is the partial tilting of the segments into the membrane (Fig. 2C, bottom). While the central portion of TM1 (from positions I38C-SL to I44C-SL, Fig. 2C) did not show major changes in dynamics, TM2 and TM3 became more mobile, and TM2 in particular, more exposed to the lipids (Fig. 2C, middle). Residues in the TM3 helix that are fully buried and isolated from water and lipids in the closed conformation (21), show a periodic increase in NiEdda accessibility in the open state (Figs. 2C, bottom, 3B). This suggests that TM3 moves away from the sevenfold symmetry axis and increases the diameter of the permeation pathway.

The location and extent of these conformational rearrangements can be visualized by mapping the differences between open and closed state data sets onto the recently refined MscS crystal structure (12,13) or its closed state model (21) (Fig. 3A). Mobility changes for the TM1 helix were largest at both of its ends (Fig. 3A and S2), as would be expected from a downward tilting of the most peripheral of TM segments. This rearrangement might represent the end effect of the transducing bilayer forces in the channel perimeter and would be in agreement with the suggestion that the tension sensor in MscS is located at both ends of the membrane/channel interface (6). Residues immediately preceding TM1 gained O_2 accessibility while simultaneously reducing NiEdda exposure (Fig. 3A). Interestingly, mapping the TM1 and TM2 environmental changes onto the crystal structure revealed a better spatial correlation than when mapped onto the closed state model (Fig. 3A). This might suggest that the crystal structure represents an intermediate gating conformation more reminiscent of the open than the closed state (22–26).

After LPC incorporation, most of TM3 spin-labeled residues become more mobile and display a periodic increase (α-helical) in accessibility to NiEdda (Fig. 3B and S4), as protein-protein contacts presumably weaken upon opening. When mapped in non-conducting models (Fig. 3A), the NiEdda-accessible face of the TM3 helix in the open state points away from the permeation pathway. This suggests that TM3 undergoes a substantial rotation about its principal axis. Moreover, the C-terminal part of the TM3 also appears to face out the permeation pathway. This accessibility change would require at least some straightening of the two TM3 segment helices, since regions immediately after the G113 kink show no measurable NiEdda accessibility in the closed conformation (Fig. 3B). This experimental evidence agrees with previous molecular dynamic simulations (21,23), as well as with an experimental study where helical formation induced by G113A and by G121A prevented inactivation and inactivation and closure, respectively (30).

The direction of the TM helices movement can be deduced from changes in individual environmental moments between the closed and open states, as shown on a helical wheel representation (Fig. 3C and S4). Calculation of the resultant angular vector differences shows that in order to explain the changes in O_2 accessibilities (A33C-SL to I39C-SL, and G41C-SL to I44C-SL), TM1 and TM2 segments must rotate about 50° and 36°, respectively, in the counterclockwise direction (Fig. S5). Furthermore, to satisfy the changes in NiEdda accessibility data, the TM3 helices not only have to translate away from the symmetry axis but also need to rotate about 130° in the counterclockwise direction (Fig. 3C). While the magnitude of the helix rotations reported might be biased by repacking of some of the spin-labeled mutants, the overall trend and direction of helix rotations (derived from the combination of data from multiple independent mutants) should not be affected. These movements provide a mechanistically feasible way to expose the helix face highlighted by residues A98C-SL, A106C-SL and G113C-SL to the permeation pathway in the open state (Fig. 3B), while defining inter-subunit contacts in the closed state. Such rotations would break a proposed hydrophobic seal responsible for stabilizing the seven helix bundle in the

closed state and serve as an energetic barrier to the ions flow (25,35). Given the diameter of NiEdda (~6 Å) and the average length of the nitroxide tether (~5 Å), the diameter of the permeation path in the open conformation should be at least 11 Å to allow unfettered diffusion of the collisional contrast agent into the open pore (22,30).

Using a computational approach that takes advantage of EPR-determined solvent accessibility restraints (36) we previously generated an EPR-based model of the closed state (21). Here, we used this as a starting conformation to model a symmetrized version of the MscS open state. First, MscS TM helices were rotated according to the changes in helical environment moments obtained from the EPR data sets. Then, pseudo-atoms representing EPR spin-label probes were attached to residues 1 to 178. Finally, MD simulations were performed in which interactions between EPR probes and pseudo-atoms representing NiEdda and O_2 were chosen to enforce the environments detected in the EPR experiments. In addition, an external cylindrical harmonic potential was applied to Cα atoms to induce channel opening (see the supplementary material for details).

The resulting MscS open model that best satisfied our experimental constraints is shown in Fig. 4A. Comparison with the closed conformation suggests three key gating mechanistic highlights: 1) the TM1 helix tilts downward and rotates to expose TM2 to the membrane, 2) Helices TM3a and TM3b move away from the permeation pathway while 3) TM3a inclines towards the plane of the bilayer, decreasing the kink angle at G113. Interestingly, residue L105 (Fig. 4B) previously forming a putative hydrophobic seal now faces away from the pore, and the narrowest part of the pore (about 11 Å in diameter) is lined by residue V99.

We have analyzed our current models for MscS closed and open conformations in light of the available experimental data. All-atom MD simulations of the open state (see supplement) predict an ionic conductance that approximates the 1 nS seen experimentally (37). Furthermore, when some of the extreme mutations that causes either loss or gain of function phenotypes (LOF and GOF, respectively) are mapped on both the closed and open models, a striking spatial correlation emerges (Fig. 4B). In either conformation, LOF mutants tend to localize at the protein/membrane interface, while GOF mutants cluster in the middle of the TM segments. The location of the LOF mutants (6) might help explain their phenotype, since specific polar substitutions could strengthen interaction with lipid head groups, increasing the energetic cost of the TM1–TM2 hairpin tilting required for channel opening. On the other hand, polar GOF substitutions in the middle of TM1 and TM2 would affect inter-helix packing, perhaps favoring the inter-helix rearrangement between TM1 and TM2 (Fig 4B) that leads to opening. Dramatic GOF phenotypes derived from mutations in the pore (38) destabilize the hydrophobic seal required to keep the channel closed, and might promote TM3 rotation.

Vertical cross-sections of the permeation pathway calculated (39) for the closed and open models and the refined MscS crystal structure (13) highlight the pore's morphological changes in the different structural snapshots during gating (Fig 4C). The MscS crystal structure shows a narrow (~6 Å) region in the intracellular side of the pore that extends 10 Å in the z-axis and has been associated with the formation of a non-conductive “vapor plug” (24–26). In our closed state model (21), this narrowing extends 25 Å towards the extracellular side of the pore, further increasing the energetic cost for ions to traverse this region. The series of TM1–TM2 tilts and TM3 rotations lead to the formation of a large 10–12 Å × 20 Å conductive pathway lined by the TM3a and TM3b segments; preliminary MD simulations show conduction of both cations and anions through this pore (Fig. S6). Interestingly, these permeation pathway cross-sections underlie the similarities between the open model and the MscS crystal structure (12,13). Except for the narrowing at the intracellular end of its pore (Fig 4C, arrows), the crystal structure could, in principle, support

ion conduction and thus might represent a post-opened, inactivated/desensitized conformation. The structural rearrangements described here clearly demonstrate a gating mechanism that is distinct from that of MscL (14,17,18), but that confirms the critical role of helix tilting in transducing bilayer deformations to generate an aqueous pathway through the membrane.

Sentence Summary

Electron paramagnetic resonance measurements in a membrane environment reveal the structural rearrangements associated with the gating mechanism of a mechanosensitive channel.

Supplementary Material

Refer to Web version on PubMed Central for supplementary material.

Acknowledgments

We thank Vishwanath Jogini, Sudha Chakrapani, H Raghuraman, and D. Marien Cortes for providing comments and experimental advice. M.S. was an associate of the Howard Hughes Medical Institute in the laboratory of David Corey. This work was supported by the NIH grants GM063617 (E.P.), P41-RR05969 (K.S.), and 1 R01 GM067887 (K.S.). Supercomputer time provided through NSF grant LRAC MCA93S028.

References

1. Levina N, et al. Embo J 1999;18:1730. [PubMed: 10202137]
2. Christensen AP, Corey DP. Nat Rev Neurosci 2007;8:510. [PubMed: 17585304]
3. Martinac B. Cell Physiol Biochem 2001;11:61. [PubMed: 11275684]
4. Pivetti CD, et al. Microbiol Mol Biol Rev 2003;67:66. [PubMed: 12626684]
5. Yoshimura K, Nomura T, Sokabe M. Biophys J 2004;86:2113. [PubMed: 15041651]
6. Nomura T, Sokabe M, Yoshimura K. Biophys J 2006;91:2874. [PubMed: 16861270]
7. Maingret F, Patel AJ, Lesage F, Lazdunski M, Honore E. J Biol Chem 2000;275:10128. [PubMed: 10744694]
8. Hayakawa K, Tatsumi H, Sokabe M. J Cell Sci 2008;121:496. [PubMed: 18230647]
9. Gottlieb P, et al. Pflugers Arch 2008;455:1097. [PubMed: 17957383]
10. Kwan KY, et al. Neuron 2006;50:277. [PubMed: 16630838]
11. Chang G, Spencer RH, Lee AT, Barclay MT, Rees DC. Science 1998;282:2220. [PubMed: 9856938]
12. Bass RB, Strop P, Barclay M, Rees DC. Science 2002;298:1582. [PubMed: 12446901]
13. Steinbacher, S.; Bass, R.; Strop, P.; Rees, DC. Structures of the prokaryotic mechanosensitive channels MscL and MscS. Part A. Elsevier Inc.; 2007. Mechanosensitive Ion Channels; p. 1-24.Current Topics in Membranes
14. Perozo E, Cortes DM, Sompornpisut P, Kloda A, Martinac B. Nature 2002;418:942. [PubMed: 12198539]
15. Perozo E, Kloda A, Cortes DM, Martinac B. Nat Struct Biol 2002;9:696. [PubMed: 12172537]
16. Sukharev S, Betanzos M, Chiang CS, Guy HR. Nature 2001;409:720. [PubMed: 11217861]
17. Gullingsrud J, Schulten K. Biophys J 2003;85:2087. [PubMed: 14507677]
18. Betanzos M, Chiang CS, Guy HR, Sukharev S. Nat Struct Biol 2002;9:704. [PubMed: 12172538]
19. Perozo E, Kloda A, Cortes DM, Martinac B. J Gen Physiol 2001;118:193. [PubMed: 11479346]
20. Gullingsrud J, Kosztin D, Schulten K. Biophys J 2001;80:2074. [PubMed: 11325711]
21. Vasquez V, et al. J Mol Biol 2008;378:55. [PubMed: 18343404]
22. Sotomayor M, Vasquez V, Perozo E, Schulten K. Biophys J 2007;92:886. [PubMed: 17114233]

23. Sotomayor M, van der Straaten TA, Ravaioli U, Schulten K. Biophys J 2006;90:3496. [PubMed: 16513774]
24. Sotomayor M, Schulten K. Biophys J 2004;87:3050. [PubMed: 15339798]
25. Anishkin A, Sukharev S. Biophys J 2004;86:2883. [PubMed: 15111405]
26. Spronk SA, Elmore DE, Dougherty DA. Biophys J 2006;90:3555. [PubMed: 16500980]
27. Koprowski P, Kubalski A. J Membr Biol 1998;164:253. [PubMed: 9691118]
28. Akitake B, Anishkin A, Sukharev S. J Gen Physiol 2005;125:143. [PubMed: 15657299]
29. Martinac B, Adler J, Kung C. Nature 1990;348:261. [PubMed: 1700306]
30. Akitake B, Anishkin A, Liu N, Sukharev S. Nat Struct Mol Biol 2007;14:1141. [PubMed: 18037888]
31. Moe P, Blount P. Biochemistry 2005;44:12239. [PubMed: 16142922]
32. Markin, VS.; Sachs, F. Thermodynamics of Mechanosensitivity. Hamill, O., editor. Elsevier Inc; 2007. Current Topics in Membranes
33. Vasquez V, Cortes DM, Furukawa H, Perozo E. Biochemistry 2007;46:6766. [PubMed: 17500538]
34. Farahbakhsh ZT, Altenbach C, Hubbell WL. Photochem Photobiol 1992;56:1019. [PubMed: 1492127]
35. Edwards MD, et al. Nat Struct Mol Biol 2005;12:113. [PubMed: 15665866]
36. Sompornpisut P, Perozo E, Roux B. Biophys J. 2007
37. Martinac B, Buechner M, Delcour AH, Adler J, Kung C. Proc Natl Acad Sci U S A 1987;84:2297. [PubMed: 2436228]
38. Miller S, et al. Embo J 2003;22:36. [PubMed: 12505982]
39. Smart OS, Neduvelil JG, Wang X, Wallace BA, Sansom MS. J Mol Graph 1996;14:354. [PubMed: 9195488]

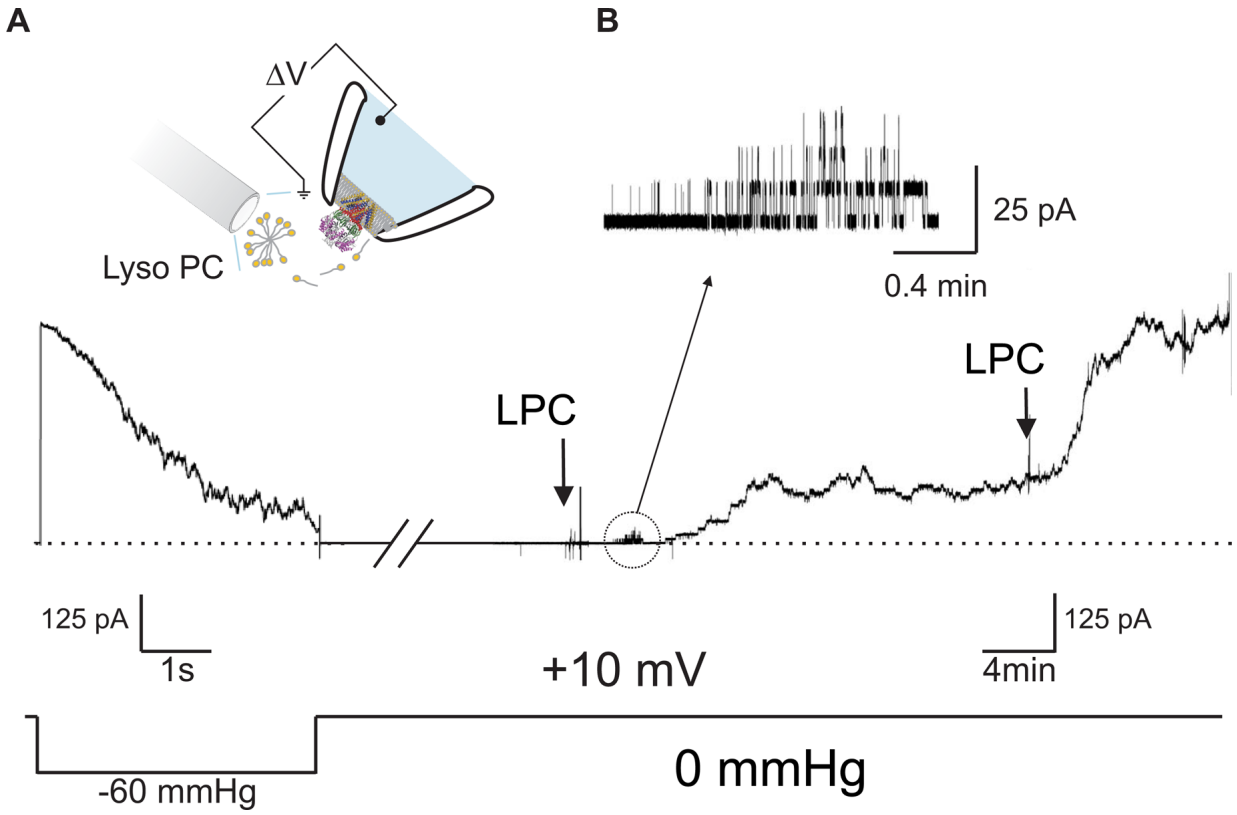

Fig. 1.

LPC incorporation permanently activates MscS. **(A)** Top, MscS orientation in the inside-out patch-clamp configuration, and perfusion of LPC micelles. Bottom, representative MscS macroscopic currents (~55 channels in the patch) activated by negative pressure (at −60 mmHg and + 10 mV) reveal the presence of a time-dependent inactivation process. **(B)** Sequential incorporation of LPC (3 μM) into the internal leaflet of inside-out patches from *E. coli* spheroplasts and in the absence of applied tension elicits spontaneous openings (after ~2 minutes). All the channels present in the patch (as determined from tension induced macroscopic currents) are activated by LPC. Inset shows single channel transitions.

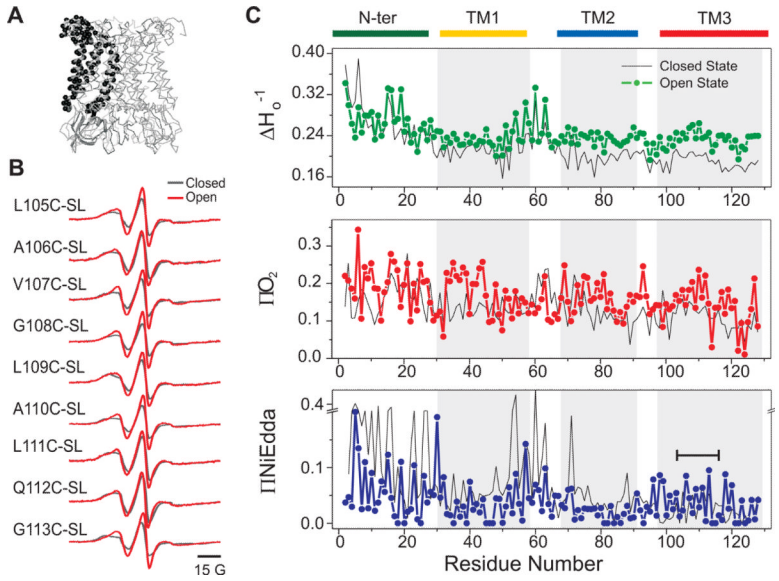

Fig. 2.

Structural rearrangements underlying channel opening. **(A)** A single MscS monomer is represented as part of the heptamer according to the MscS closed state model obtained from the EPR based refinement (21). The aminoacid residues subjected to cysteine scanning mutagenesis in the present study are shown as black spheres. **(B)** Representative X-band EPR spectra of consecutively spin-labeled mutants along the permeation pathway (TM3). Black and red traces were obtained from channels in the closed and open conformations, respectively. All spectra were obtained from samples at the same protein to lipid ratio, and using a dielectric resonator with the microwave power set to 2 mW. Channel opening was obtained in DOPC:POPG + 25 mol % LPC vesicles. **(C)** Residue-specific environmental parameter profiles obtained in the open and closed (black curve) conformations for the N-terminal and TM segments: mobility parameter ΔH_o^{-1} (top, green curve), O_2 accessibility parameter ΠO_2 (middle, red curve), and NiEdda accessibility parameter ΠNiEdda (bottom, blue curve). Bar covers the region for which EPR spectra are shown in 2B. Gray areas represent the TM segment assignment derived from the MscS crystal structure (12,13).

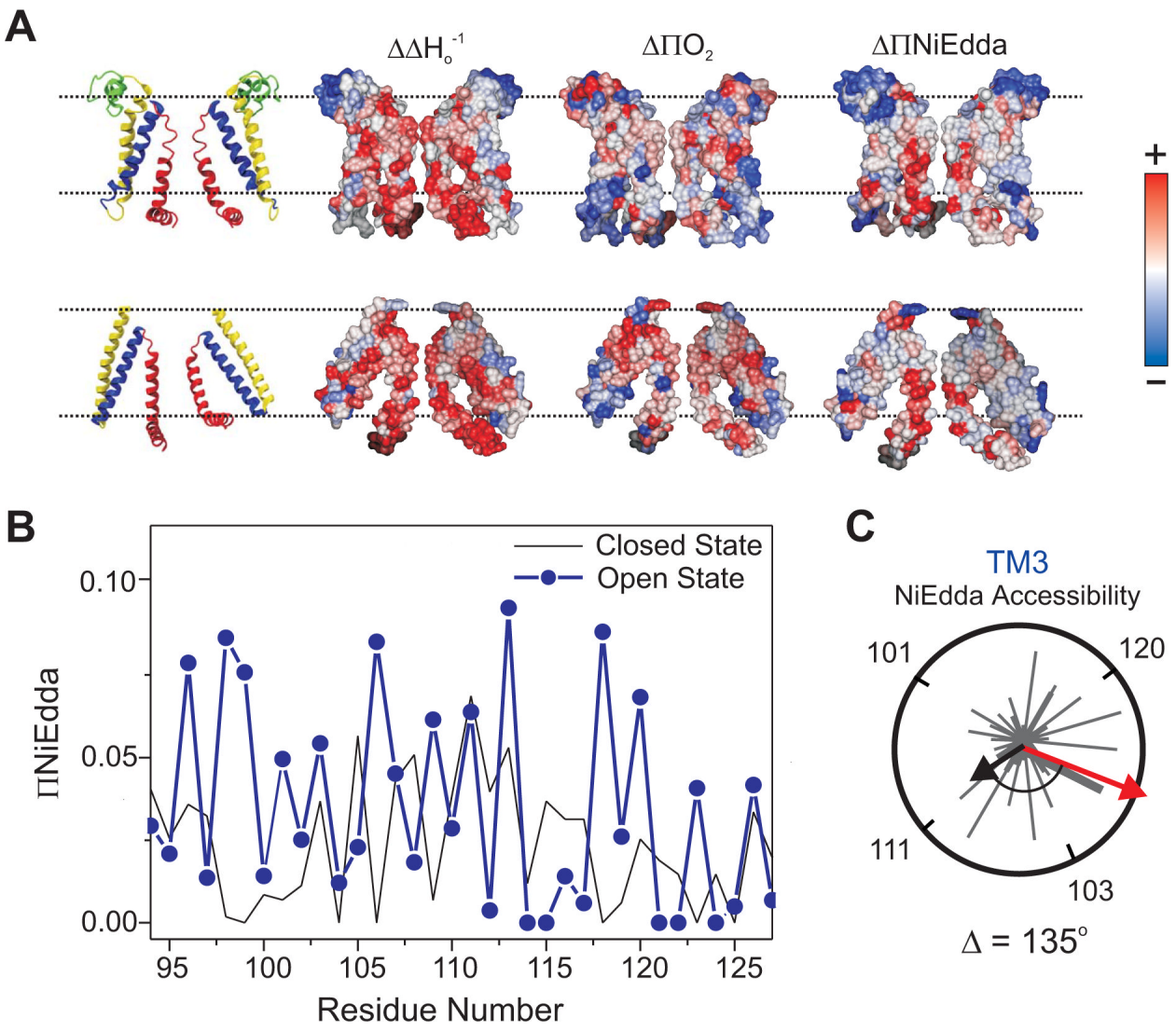

Fig. 3.

Extent and direction of environmental parameter changes upon MscS opening. **(A)** Changes in local dynamics and solvent accessibilities mapped onto molecular surfaces of the closed state EPR-based model (top) and the crystal structure (bottom). The leftmost panel shows ribbon representations of MscS (two subunits are shown for clarity) where individual TM segments are color-coded as follows: N-terminus, green, TM1, yellow; TM2, blue; and TM3, red. From left to right: Mobility ($\Delta\Delta H_o^{-1}$), Oxygen accessibility ($\Delta\Pi O_2$), and NiEdda accessibility ($\Delta\Pi$NiEdda) changes. **(B)** ΠNiEdda residue-specific environmental parameter profile for the TM3 helix obtained in the open (blue curve) and closed (black curve) conformations. **(C)** Vector analysis of TM3 environmental data in the open conformation. ΠNiEdda parameters have been superimposed in a polar coordinate. Resultant moments for the closed (black arrow) and open (red arrow) conformations were calculated from the accessibilities.

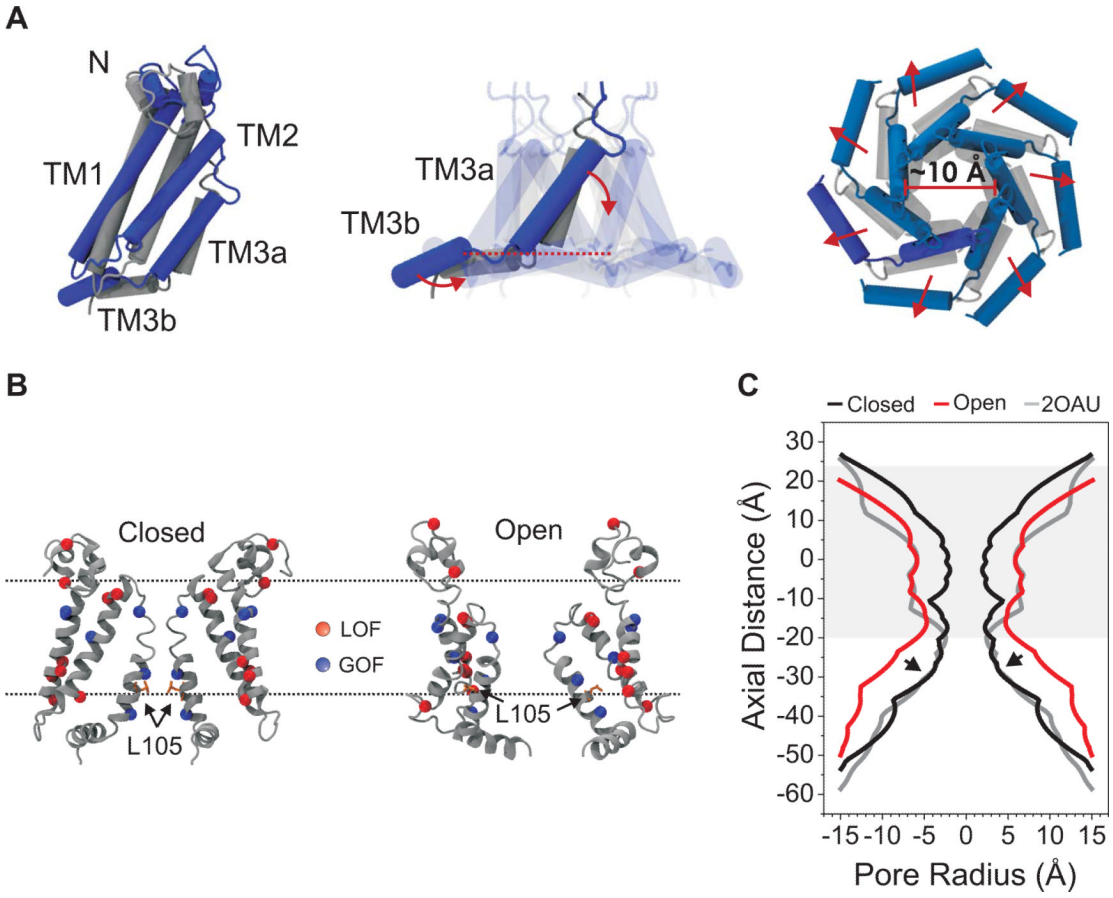

Fig. 4.

A structural model for MscS gating in lipid bilayers. **(A)** Side and extracellular views of the structural rearrangements leading to the open conformation. Left, a single MscS subunit is highlighted in blue and gray for the open and closed states, respectively. Middle, TM3a and TM3b helices (residues 94–128 and 91–128 for the closed and open models, respectively). Right, extracellular view of the pore. Helical movements are illustrated by red arrows. **(B)** GOF (blue) and LOF (red) mutants mapped onto two subunits of MscS closed (left) and open (right) conformation models. GOF: I39N and I78N (6), V40D (42), T93R, A102P, and L109S (40). LOF: V6C and A19C (21), I48D/S49P (40), A51N, L55N, F68N, A85N, and L86N (6). Residue L105 (arrows) is shown in stick representation. **(C)** Cross-sectional area of MscS pore in the closed, open, and crystal conformations. Each cross-section was obtained from the calculated surface using the program HOLE (39).